

Research Paper

SoHO/EIT, Stereo-A, and SDO/AIA View for Solar Coronal Differential Rotation

Zahra Shokri^{*1} · Nasibe Alipour² · Hasan Rezaei³ · Mehdi Simiari⁴ · Hossien Safari⁵

¹ Department of Physics, Faculty of Science, University of Zanjan, University Blvd., Postal Code 45371–38791, Zanjan, Iran;

*email: shokri.zahra@znu.ac.ir

² Department of Physics, University of Guilan, Rasht, 41335–1914, Iran;

email: nasibealipour@gmail.com

³ Department of Geography, Faculty of Basic Sciences, Imam Ali Nazaja University, Postal Code: 1317893471, Tehran, Iran;

email: rezaei_hasan63@yahoo.com

⁴ Department of physics, Faculty of Science, Imam Ali University, Postal Code: 1317893471, Tehran, Iran;

email: mahdi.simiari@gmail.com

⁵ Department of Physics, Faculty of Science, University of Zanjan, University Blvd., Postal Code 45371–38791, Zanjan, Iran;

email: safari@znu.ac.ir

Received: 24 April 2025; Accepted: 22 June 2025; Published: 29 June 2025

Abstract. Differential rotation of the solar corona is challenging to the nature of short-wavelength emissions. In this study, we aim to measure solar coronal differential rotation from different perspectives using observations from SoHO/EIT at 195 Å, Stereo-A/EUVI at 195 Å, and SDO/AIA at 193 Å on June 1st, 2010. To achieve this, we apply a method based on Zernike Moments and Support Vector Machine (SVM) to identify and track coronal bright points (CBPs) over a 10 hour observation period. In the heliographic coordinate system, we determine the angular velocity of the corona by fitting a linear time-dependent function to the central meridian distance of each CBP. By analyzing a collection of CBPs in the solar equatorial central region (within $\pm 50^\circ$ in longitude and latitude) from each perspective, we obtain the equatorial rotation rate (A) and the latitudinal rotation gradient (B). The results indicate values of 14.32, 14.54, and 14.51 $^\circ\text{day}^{-1}$ with -2.93, -4.03, and -3.16 $^\circ\text{day}^{-1}$ for SoHO, Stereo-A, and SDO, respectively.

Keywords: Solar Rotation, Differential Rotation, Ultraviolet Bright Points, SVM, Zernike Moments.

1 Introduction

Long-lived rotational and meridional flows are key features of the solar cycle. The study of differential rotation provides an observational framework for theoretical models of the solar convective zone and magnetohydrodynamic dynamo processes, which play a crucial role in generating and sustaining the Sun's magnetic field and its overall activity [1–3]. A much

* Corresponding author

This is an open access article under the CC BY license.



weaker meridional flow accompanies differential rotation, moving toward the Sun's poles at approximately 20 ms^{-1} [4]. Previous studies indicate that solar rotation, with its equatorial and differential components, governs the evolution and structure of the magnetic field from the solar interior (beneath the photosphere) to the outer atmospheric layers [5,6]. Such changes in the structure and connectivity of the magnetic field enable the transport of internal energy into the solar atmosphere, where it is stored and released in the form of magnetic energy. Through mechanisms such as magnetic reconnection and magnetohydrodynamic waves, this energy is released in various forms [7]. Several methods have been employed to study solar differential rotation, including tracking atmospheric features [8,9], spectroscopic measurements [10,11], flux modulation [12–14], and seismic segmentation of p-modes [15]. One of the earliest techniques involves tracking solar features such as sunspots, magnetic fields, and small/large-scale coronal structures to determine the rotation parameters A (equatorial rotation) and B (latitudinal rotation gradient).

Sudar et al. (2015) analyzed the differential rotation of the Sun by tracking CBPs from SDO/AIA images over two days in 2011 at a 10-minute cadence. They reported rotational parameters of 14.62 and $-2.02 \text{ }^\circ\text{day}^{-1}$ [9]. Similarly, Wöhl et al. (2010) tracked small CBPs using SoHO/EIT data from 1998 to 2006 at a six-hour cadence, obtaining rotation parameters of 14.529 and $-3.03 \text{ }^\circ\text{day}^{-1}$ using an automated method [16].

To characterize solar differential rotation independently of Earth's orbital effects, measurements are typically conducted in the sidereal frame, where rotation rates are referenced to the fixed background of distant stars. Various solar indices, including sunspots [17], flares [18], prominences [19], and extreme ultraviolet bright points [9], have been used to study differential rotation through observational data.

Sunspots are widely used tracers for determining solar rotation due to their clear visibility and centuries-long observational record. With over 400 years of continuous observations—ranging from visual to photographic and CCD-based detections—sunspot datasets provide standardized heliographic positions enabling long-term rotation studies. Their global monitoring minimizes data gaps, and the lifetime of some sunspot groups allows tracking across multiple solar rotations. However, limitations exist: Sunspots are confined to low and mid-latitudes, offering no data for polar rotation. Their latitudinal distribution also varies with the solar cycle. Additionally, variability in sunspot group morphology complicates coordinate determination, especially for complex groups. Finally, intrinsic motions and structural evolution of sunspot groups introduce non-rotational components in positional changes, which must be accounted for during analysis. Therefore, tracking small-scale brightening features, such as extreme ultraviolet bright points, blinkers, and small magnetic structures, which are present across all latitudes and longitudes, is crucial for measuring differential rotation. These transient events play a fundamental role in mass and energy transfer in the solar atmosphere [9,20–25].

CBPs are small, localized features in the solar corona that are generally associated with magnetic activity in the Sun's atmosphere. These points are typically linked to small-scale magnetic bipoles, where regions of opposite magnetic polarity are restricted to a limited area on the solar surface. Identifying CBPs has been an ongoing challenge due to their small size, dynamic nature, and ability to evolve rapidly under varying solar conditions [26]. Early studies suggested that these features might be related to micro flares or the mechanisms of coronal heating, but it was only with the advancement of high-resolution solar observations, particularly in extreme ultraviolet (EUV) and X-ray wavelengths, that their association with solar transients like blinkers became more evident [27]. In this context, Shokri et al. (2022) investigated the relationship between CBPs and blinkers, demonstrating that these features frequently form near regions with dynamic solar activity and EUV emissions [22]. The development of more precise instruments, such as the SDO and Stereo spacecraft, has

significantly improved our ability to observe these features in detail, thus advancing our understanding of the Sun’s magnetic activity at small scales [28].

One of the main challenges in studying CBPs has been the difficulty in consistently identifying and tracking these features due to their transient nature and the large volume of data generated by solar imaging instruments. To address this, recent advancements in automated image processing techniques have become crucial. Methods based on invariant features, such as Zernike Moments, have proven effective in extracting features from solar images [20,24]. By combining these mathematical tools with machine learning algorithms like SVM, researchers have been able to automate the process of CBP identification, enabling efficient analysis of large datasets [29,30]. This approach not only reduces the human effort required for feature identification but also provides a more consistent and systematic method for tracking CBPs across different observational conditions.

Recently, the Zernike Moments have been widely investigated to identify and track of solar atmospheric small scale features such as mini dimming and mini CMEs [24,31,32], brightenings [20,22,23,29,30,33,34]. Also, the Zernike Moments extracted from solar active regions were used to accurately predict flares and classification of flaring and non flaring active region [20,35]. The Zernike Moments were also applied to classify galaxy images into spiral, elliptical, and irregular types from galaxy zoo 2 data set [36]. The zemo package was developed by Safari et al. (2024) [37] and available at GitHub <https://github.com/hmddev1/ZEMO> and PyPI <https://pypi.org/project/ZEMO/1.0.0/>.

This paper is organized as follows: Section 2 discusses the analysis of solar data, Section 3 gives methods including the identification and tracking of CBPs and determining solar differential rotation parameters. Section 4 presents the obtained results and their implications. Section 5 summarizes the concluding remarks.

2 Data Analysis

To study the differential rotation velocity of the Sun, we utilize images from the SDO/AIA satellite at a wavelength of 193 Å, the Stereo-A satellite of 195 Å, and the SoHO/EIT instrument at a wavelength of 195 Å on June 1st, 2010. The dataset consists of observations over a single day with a 12-minute cadence for SoHO/EIT and 10-minute cadence for Stereo-A and SDO/AIA to first 10 hours. To minimize the effects of the solar background, only regions within ± 50 degrees in latitude and longitude are analyzed.

The EIT on the SoHO spacecraft has been instrumental in observing the Sun’s outer atmosphere since its launch in 1995. It captures images in multiple EUV wavelengths, including 171, 195, 284, and 304 Å, providing critical insights into solar activity. Although EIT’s initial cadence was 12 minutes, its role diminished with the advent of more advanced instruments, yet it continued to provide valuable data until 2010. The EIT instrument offers a spatial resolution of 2.4 arcseconds and image dimensions of 1024×1024 pixels.

The EUVI aboard the Stereo spacecraft, launched in 2006, captures stereoscopic images of the solar corona from two vantage points. This instrument observes the Sun in EUV wavelengths such as 171, 195, 284, and 304 Å, offering a unique 3D view of solar activity. EUVI has been crucial for studying solar eruptions, coronal mass ejections, and their interactions with space weather. The EUVI instrument has a spatial resolution of 1.2 arcseconds and image dimensions of 2048×2048 pixels.

The AIA on SDO, launched in 2010, provides high-resolution images of the Sun’s atmosphere across a broad range of EUV wavelengths (1600 to 94 Å). AIA’s rapid cadence of 12 seconds and its spatial resolution of 0.6 arcseconds allow for continuous, real-time observations, revolutionizing our understanding of solar phenomena like solar flares, coronal mass

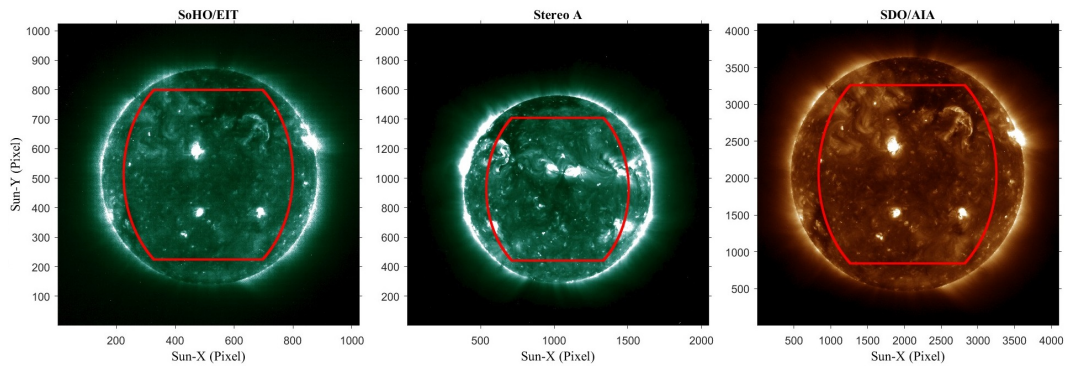


Figure 1: Extreme ultraviolet images observed by SoHO/EIT at 195 \AA (left panel), Stereo-A/EUVI at 195 \AA (middle panel), and SDO/AIA at 193 \AA (right panel) of the Sun on 1 June 2010 from three space-based instruments, with the study area highlighted in red, corresponding to ± 50 degrees heliographically to reduce projection effects.

ejections, and coronal heating. The AIA instrument has image dimensions of 4096×4096 pixels.

Figure 1 shows ultraviolet images of the Sun on 1 June 2010, taken by three different instruments: SoHO/EIT, Stereo-A/EUVI, and SDO/AIA. The region outlined in red corresponds to a heliographic range of ± 50 degrees in both latitude and longitude. All analyses in this study are restricted to this central region of the solar disk in order to minimize projection effects near the solar limb.

3 Methodology

3.1 Identification of CBPs

In recent years, various methods have been employed to identify solar events, among which intensity thresholding based on a trial-and-error approach has been one of the most commonly used techniques. In this method, solar features are detected by defining a specific intensity threshold. However, due to the irregular fluctuations and dynamic nature of intensity across different solar structures, the use of a fixed threshold often lacks sufficient accuracy and can lead to significant errors in the identification process. Therefore, the development and application of more intelligent and flexible approaches for more accurate analysis of such phenomena have become essential.

In order to identify CBPs at the 193 wavelength this study employs a modified version of the automated coronal event detection algorithm originally introduced by Alipour and Safari (2015) and subsequently refined by Shokri et al. (2022, 2024) [20,22,23]. The identification procedure is based on the extraction of Zernike Moments and classification using a SVM. A detailed description of the methodology is provided in the following steps:

Zernike orthogonal moments are widely utilized as effective feature extractors in image processing tasks. These moments are invariant under rotation around the origin and exhibit low sensitivity to noise and reconstruction errors [37]. The Zernike Moment kernel is defined within a unit circle in polar coordinates, with the center of the image aligned to the center of this circle. The complex two-dimensional Zernike Moment of order p and repetition q is computed by normalizing the pixel coordinates within each segmented region through a

linear transformation to the range $[0,1]$. In this process, the center of each segmented region is considered the origin, and the corresponding pixel coordinates are mapped onto the unit circle. In the conventional approach, assuming a square image of size $N \times N$, the region of interest is peripherally mapped onto the unit circle, and pixels lying outside this circle are excluded from the moment calculation.

Higher-order Zernike Moments are capable of capturing finer structural details of the image. However, in the present study, Zernike Moments of order 5 are employed, as the extraction of fine-grained features is not critical for the intended application. This level of approximation has been shown to be sufficient for effective image reconstruction, as demonstrated in Figure 1 of Shokri et al. (2022) [22].

With advancements in solar data technology, there is an increasing need for high-precision image processing, storage, and classification algorithms. The SVM algorithm was introduced by Vapnik in 1963 as a pattern recognition method and belongs to the family of classification algorithms [38]. In SVM, data group separation is achieved by fitting a linear function of a specific form, which enables the distinction between two or more classes. Notably, this linear separation applies mainly to two-dimensional spaces, while in higher-dimensional spaces, hyperplanes are required. For example, in a two-dimensional space, the corresponding hyperplane is a line, while in a three-dimensional space, it becomes a two-dimensional plane. The optimal separation is determined by maximizing the margin between the data points and the decision boundary. This type of classification is known as linear partitioning for linearly separable data. However, if the data are non-linearly distributed, as in the events analyzed in this study, a kernel function is first applied to transform the data into a higher-dimensional space where linear separation is possible, after which classification is performed by the SVM algorithm.

In the first step of this study, Zernike Moments of order 5 are extracted for each box corresponding to the positions of visually identified coronal features, incorporating morphological, intensity, and geometric shape information. Alipour et al. (2019) demonstrated that Zernike Moments with $p < 10$ can effectively reconstruct all shapes of active regions [39]. Additionally, moments are extracted for regions devoid of such phenomena, including large-scale active regions, extended loops, and dark quiet-Sun areas. For instance, CBPs are selected based on the following criteria: morphologically, they appear as small bright loops or compact active regions; size-wise, they range from 4.8 to 60 arcseconds; and in terms of intensity, they exhibit a peak brightness relative to the background [20]. These two sets of features serve as input data for the machine learning algorithm, which is trained to classify into two categories: events and non-events. Approximately 1,000 events and 1,000 non-events are randomly selected for the period from 2011 to 2019 based on Shokri et al. 2022 [22].

According to the detection algorithm, an initial pixel is selected on the solar disk, and a 12×12 arcsecond box is centered at this pixel. Within this box, a secondary box is defined at the location of maximum intensity, with dimensions adjusted based on the event size and the training set's Zernike Moments (here, 50×50 arcsecond for small CBPs and 90×90 arcsecond for larger ones). If the features extracted in this box (reconstructed Zernike image) match the training of SVM algorithm, its location is stored as a coronal phenomenon. Otherwise, the algorithm moves to the next pixel, continuing until the entire solar disk is examined. To prevent duplicate identification and remove redundant overlapping detections, the region-growing algorithm is applied. Originally introduced by Adams and Bischof (1994), this algorithm has been widely used in real-world image processing due to its efficiency [40]. This algorithm expands a selected region by adding neighboring pixels within a defined intensity threshold range. As a region-based segmentation method, it also functions as a cell-based classification approach by selecting initial seed points at event brightness centers.

The algorithm evaluates adjacent cells from the initial brightness center and determines whether they should be included in the event region. The steps of the region-growing algorithm are as follows:

1. Select the cell with the highest intensity as the seed point.
2. Examine neighboring cells and add them to the region if they are similar to the seed intensity.
3. Repeat step 2 for newly added cells until no further cells meet the criteria.

Finally, the coordinates (x, y) of the peak intensity within the event area (determined by the region-growing algorithm) are stored as the final bright point position.

Following the identification of bright points at the corona in the SDO/AIA, the Stereo-A with a 10-minute cadence, and the SoHO/EIT with a 12-minute cadence, their spatial tracking is performed. One of the key concerns addressed in the analysis by Shokri et al. (2024) is the reliability of the CBP tracking algorithm when applied with a 10-minute cadence, especially considering that earlier studies [20,33] have shown that the lifetime of some brightening features can be shorter than 10 minutes. In such cases, if two short-lived CBPs appear at nearly the same location in consecutive frames, the algorithm may incorrectly identify them as a single continuous feature. To resolve this ambiguity, Shokri et al. (2024) employed Zernike Moments to compare the structural similarity between features in successive frames. By analyzing the differences between similar and dissimilar CBPs, they defined a discriminant threshold and modified the tracking algorithm accordingly. This refinement significantly improved the accuracy of lifetime detection for CBPs in datasets with a 10-minute cadence (as defined in Figure 2,3 Shokri et al.2024) [23].

3.2 Solar Differential Rotation Calculation

To analyze differential rotation, the first step here is to convert the pixel coordinates (x, y) of a CBP on the solar disk into the heliographic coordinate system, longitude (CMD, l) and latitude (b). This transformation is performed using the WCS-CONVERT-FROM-COORD function in the IDL software package. In this process, the B-angle must also be corrected. The B-angle describes the Earth's position relative to the solar equatorial plane. It indicates how much the observer on Earth is looking north or south of the Sun's equator. This angle varies throughout the year because Earth's orbit is not perfectly aligned with the Sun's equatorial plane, typically ranging between ± 7.25 degrees. If the B-angle is not corrected, solar features such as sunspots or CBPs may appear to follow different trajectories, while in reality, this effect is due to our changing viewing angle. Failure to account for the B-angle correction can introduce systematic errors in the calculated rotation rates at different solar latitudes.

Now, to derive the sidereal rotation velocity from the apparent longitudinal motion of CBPs, a linear regression approach is employed to estimate the slope of their movement over time. In the linear least-squares method, we aim to fit a straight line of the form: $y = a + cx$ to a given set of experimental data points (x_i, y_i) , for $i = 1, 2, \dots, N$. The goal is to determine the coefficients a and c such that the sum of the squared residuals is minimized:

$$\chi^2(a, c) = \sum_{i=1}^N (y_i - a - cx_i)^2. \quad (1)$$

To minimize χ^2 , we take partial derivatives with respect to a and c and set them to zero:

$$\frac{\partial \chi^2}{\partial c} = -2 \sum_{i=1}^N (y_i - a - cx_i) = 0, \quad (2)$$

$$\frac{\partial \chi^2}{\partial a} = -2 \sum_{i=1}^N x_i (y_i - a - cx_i) = 0. \quad (3)$$

From the first equation, we obtain:

$$\sum y_i = aN + c \sum x_i, \quad \Rightarrow \quad a = \frac{\sum y_i - c \sum x_i}{N}. \quad (4)$$

This provides the best-fit value of a once c is known. Solving the system of equations:

$$\sum y_i = aN + c \sum x_i, \quad (5)$$

$$\sum x_i y_i = a \sum x_i + c \sum x_i^2, \quad (6)$$

we can eliminate a and solve for c :

$$c = \frac{N \sum x_i y_i - \sum x_i \sum y_i}{N \sum x_i^2 - (\sum x_i)^2}. \quad (7)$$

These are the closed-form solutions for the linear regression parameters a and c , which are widely used in both theoretical derivations and practical data analysis, including in solar physics.

In solar rotation studies, especially using the tracer method (e.g., CMD vs. time), the two fit parameters have the following interpretations:

The slope c is the key result, representing the synodic rotation velocity of a solar feature such as a sunspot or bright point. The intercept a is merely the starting CMD and has no bearing on the rotational dynamics.

Now, to calculate the differential rotation velocity, we use equation (7),

$$\omega_{\text{syn}} = \frac{N \sum_{i=1}^N l_i t_i - \sum_{i=1}^N l_i \sum_{i=1}^N t_i}{N \sum_{i=1}^N t_i^2 - (\sum_{i=1}^N t_i)^2}, \quad (8)$$

where N represents the total number of images for a single CBP during its lifetime in the tracking process.

To study the rotational motion of the Sun from an Earth-based perspective, it is important to distinguish between two types of rotational velocities: the apparent velocity of the Sun relative to the Earth, known as the synodic rotation rate, and the actual velocity of the Sun relative to the fixed stars, referred to as the sidereal rotation rate. Due to Earth's orbital motion around the Sun, an Earth-based observer perceives the Sun rotating slower than it actually does. Therefore, it is necessary to use relationships that account for Earth's motion to convert between these two velocities.

One of the simplest relationships is expressed as:

$$\omega_{\text{sid}} = \omega_{\text{syn}} + \bar{n}. \quad (9)$$

In this equation, ω_{sid} represents the actual or sidereal rotation rate of the Sun in degrees per day, while ω_{syn} denotes the apparent rotation rate of the Sun relative to Earth in the same

units. The term \bar{n} represents the mean angular velocity of Earth's orbit around the Sun, which is obtained by dividing 360° by the length of the sidereal year (approximately 365.25 days), resulting in a value of about $0.9856^\circ \text{day}^{-1}$. This relation assumes that Earth's orbit is uniform and follows a circular path, neglecting any geometric or oscillatory effects.

Next, to improve accuracy, the instantaneous angular velocity of Earth is used instead of the mean orbital velocity. This leads to the following equation:

$$\omega_{\text{sid}} = \omega_{\text{syn}} + \omega_{\text{Earth}}. \quad (10)$$

Here, $\omega_{\text{Earth}} = \frac{\bar{\omega}_{\text{Earth}}}{r^2}$ represents the instantaneous angular velocity of Earth in its orbit around the Sun, which can be calculated at any given moment using astronomical ephemerides. The parameters r can be obtained from NASA JPL Horizons¹ by selecting "Observer ephemeris type" as "Observer range & range-rate" and the parameter $\bar{\omega}_{\text{Earth}}$ is equal to $0.9856^\circ \text{day}^{-1}$. As a result, the relation is modified as follows:

$$\omega_{\text{sid}} = \omega_{\text{syn}} + \omega_{\text{Earth}} \cos \Theta. \quad (11)$$

Here $\cos \Theta$ accounts for the effective component of Earth's motion in the Sun's equatorial plane. To compute the angle Θ , celestial geometry between the ecliptic plane and the Sun's equator is utilized

$$\tan \Theta = \tan i \cos(\Lambda_0 - \Omega). \quad (12)$$

To account for the effective component of Earth's orbital motion, a specific angle, Θ , must be considered, which lies between the Earth's velocity vector and the Sun's equatorial plane. This angle ensures that only the portion of Earth's motion that truly affects the Sun's apparent rotation is included in the calculation. In Equation 12, i is the inclination of the Sun's equatorial plane relative to the ecliptic plane, which is approximately 7.25 degrees. Λ_0 represents the geocentric longitude of Earth in its orbit, or the position of Earth relative to the Sun from the center of the Sun. The parameters Λ_0 can be obtained from NASA JPL Horizons by selecting "Observer ephemeris type" as "Observer ecliptic lon. & lat.". Ω is the longitude of the Sun's ascending node on the ecliptic, where the Sun's equatorial plane crosses from south to north: $\Omega = 73^\circ 40' - 25.50''(t - 1850)$, here t is the year under consideration.

In this study, a new relation is proposed to improve the accuracy by more precisely correcting the effective component of Earth's motion in the direction of the Sun's rotation. The final form of the relation is:

$$\omega_{\text{sid}} = \omega_{\text{syn}} + \omega_{\text{Earth}} \frac{\cos^2 \Theta}{\cos i}. \quad (13)$$

In this equation, the term $\frac{\cos^2 \Theta}{\cos i}$ offers higher accuracy compared to because it corrects for both the horizontal component of Earth's velocity vector and the inclination of the Sun's equatorial plane relative to the ecliptic. As a result, only the effective component of Earth's orbital motion in the direction of the Sun's rotation is included in the calculation. Numerical computations in this study demonstrate that this new relation aligns more closely with the precise data from astronomical ephemerides and reduces millisecond discrepancies between model predictions and real data.

To compute the uncertainty in synodic velocities, we use the following equation:

$$SE = \frac{s}{\sqrt{\sum_{i=1}^N (t_i - \bar{t})^2}}, \quad (14)$$

¹<http://ssd.jpl.nasa.gov/?horizons>

where \bar{t} represents the mean lifetime of a CBP, and s is calculated using the following formula:

$$s = \sqrt{\frac{\sum_{i=1}^N (t_i - \bar{t})^2 - \frac{(\sum_{i=1}^N (t_i - \bar{t}))(t_i - \bar{t})^2}{\sum_{i=1}^N (t_i - \bar{t})^2}}{N - 2}},$$

where \bar{l} denotes the mean longitude of a CBP. The meridional velocity of the Sun is determined using a least-squares linear approach, based on the central latitude of a CBP:

$$\omega_{\text{mer}} = \frac{N \sum_{i=1}^N b_i t_i - \sum_{i=1}^N b_i \sum_{i=1}^N t_i}{N \sum_{i=1}^N t_i^2 - (\sum_{i=1}^N t_i)^2}. \quad (15)$$

Once again, the standard error of the meridional velocity is calculated.

The precise altitude of CBPs above the solar photosphere remains uncertain. Various methods have been developed to correct for the altitude effects of CBPs on rotational measurements [15–17]. One such method, a statistical approach introduced by Sudar et al. (2016), assumes that the solar rotation profile remains constant with respect to the central meridian distance. This study adopts a similar iterative procedure, outlined as follows:

- The solar surface is divided into latitudinal bands of 10 degree.

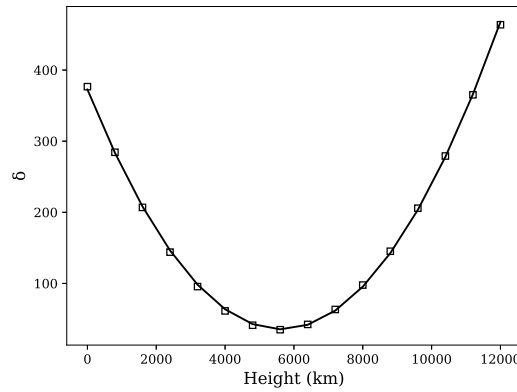


Figure 2: Variation of the δ function, as defined in Equation (20), with trail height h above the solar photosphere. The minimum value of δ occurs at 5627 km, indicating the height at which the discrepancy characterized by δ is minimized (taken from Shokri et al. 2024).

- For a sequence of altitudes (h) illustrated in Figure 2, the corrected beta parameter is computed. Consequently, the latitude, sidereal velocity, and standard error of sidereal velocity for all bright points within each segment are adjusted.

For a sequence of trial heights h , the corrected projection factor β is computed using the following equation [20].

$$\beta^2 = \frac{(\frac{h}{R_{\odot}} + 1)^2 - \sin^2 b^*}{\cos^2 b^*}, \quad (16)$$

where R_{\odot} represents the solar radius.

- The corrected latitude (b) and rotational velocity (ω) are calculated via the following equations:

$$\cos b = \frac{\beta \cos b^*}{\sqrt{\beta^2 \cos^2 b^* + \sin^2 b^*}}, \quad (17)$$

$$\omega = \frac{\omega_{\text{sid}} \cos l^*}{\sqrt{\beta^2 - \sin^2 l^*}}, \quad (18)$$

where ω_{sid} , b^* and l^* represent the measured rotational velocity, longitude, and latitude, respectively. The uncertainty in the rotational velocity is corrected in the same manner.

- For the corrected rotational velocity and solar longitude in each segment, the following function is fitted [9,45].

$$\omega_p(A, B, b) = A + B \sin^2 b, \quad (19)$$

where A and B represent the equatorial rotation rate and the latitudinal rotational gradient, respectively. Thus, we can compare the rotational parameters (A and B) for the i segment with the rotational profile in the central segment, defined within -5 to +5 degree of the central meridian. The parameters A_c and B_c correspond to the rotation parameters of the central segment.

The corresponding function (δ) for comparing the central segment's rotation with other segments at a given test altitude is given by:

$$\begin{aligned} \delta &= \sum_i \int_0^{\pi/2} \left(\omega_p(A_i, B_i, b) - \omega_p(A_c, B_c, b) \right)^2 db, \\ \delta &= \sum_i \left(\frac{\pi}{2} w_{A_i} (A_i - A_c)^2 + \frac{\pi}{4} \sqrt{w_{A_i} w_{B_i}} (A_i - A_c)(B_i - B_c) + \frac{3\pi}{16} w_{B_i} (B_i - B_c)^2 \right), \end{aligned} \quad (20)$$

The calculation is performed, where w_{A_i} and w_{B_i} are the weights corresponding to the standard error of the fit for A_i and B_i , respectively [23,25,41–44].

- The above steps are applied at various altitudes above the photosphere, ranging from 0 to 12,000 km, to find the minimum value of the function (δ) at a specific altitude.

Figure 2 illustrates the variation of the delta function with a series of different altitudes above the solar photosphere. The figure shows the parabolic behavior of the δ function with a minimum at an altitude of 5,627 km. The minimum value of the function at 5,627 km indicates that the bright points are located above the photosphere at this altitude. Therefore, using Equations 17 and 18, the latitude and rotational velocity of the CBPs are corrected for an altitude of 5,627 km.

Flowchart (Figure 3) illustrates the overall procedure for identifying and tracking CBPs and deriving the solar rotation velocity. The method includes preprocessing of EUV images, feature identification using a region-growing algorithm and SVM classifier, temporal tracking, and coordinate transformation to heliographic frames. Finally, height correction and differential rotation fitting are applied to extract the rotation parameters.

4 Results

In this study, the solar rotation velocity is investigated using the tracking of CBPs. Data analysis is based on images obtained from three different instruments: the EIT instrument

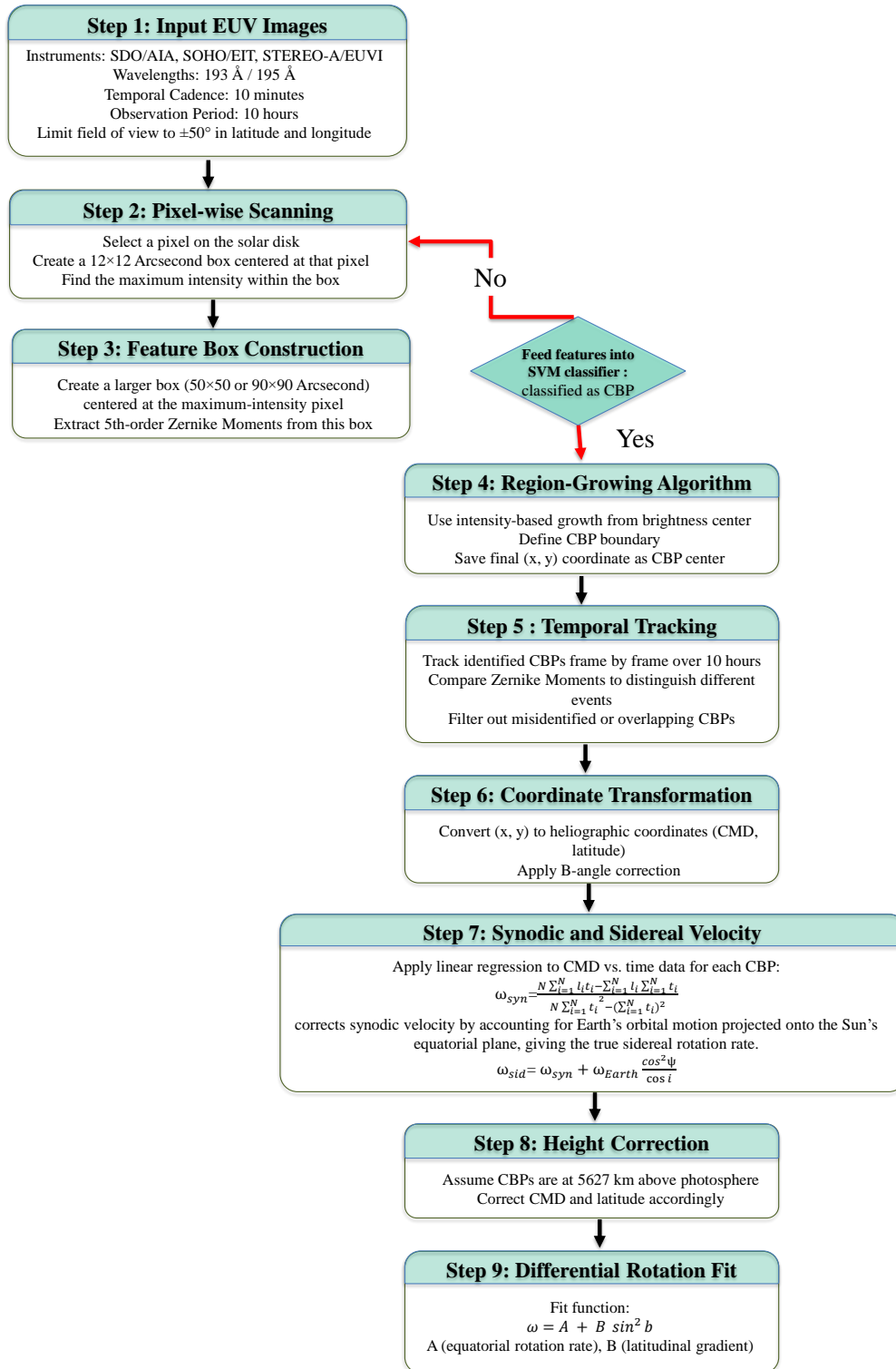


Figure 3: Flowchart of the steps for CBP identification, tracking, and solar rotation velocity calculation.

on the SoHO spacecraft, the EUVI instrument on the Stereo-A spacecraft, and the AIA instrument on the SDO spacecraft. The differences in the technical specifications of these instruments, particularly in spatial resolution, image dimensions, and temporal sampling methods, have a direct impact on the quality and accuracy of the results obtained from analyzing the rotation of CBPs.

The EIT instrument, has significant limitations. In addition to the lower quality images compared to the other two instruments, the data from this instrument suffers from irregular and discontinuous temporal sampling. This issue is particularly exacerbated during different time periods, with only one image available on certain days. Such limitations effectively prevent the precise and continuous tracking of CBPs, leading to ambiguity and significant errors in the matching process between successive images. Under these conditions, the likelihood of mistakenly identifying and tracking a bright point as the initial CBP increases. This major weakness in the EIT data not only complicates the tracking process but can also significantly reduce the accuracy of the solar rotation parameters.

In contrast, the data extracted from the EUVI instrument on the Stereo-A spacecraft, has allowed for more accurate identification and tracking of CBPs. Additionally, the AIA instrument on the SDO spacecraft, with highly regular and continuous temporal sampling, has provided the most accurate data. These characteristics have led to increased stability and accuracy in the results related to the rotation velocity of the bright points in the data from these two instruments.

The solar rotation velocity is investigated using the tracking of CBPs applying the automatic identification and tracking algorithm for CBPs on EIT at 195 Å images with cadence of 12-minute, we detect 142 CBPs in the central equatorial region (± 50) solar disk images to contribute the solar rotation calculations. The algorithm finds 264 CBPs for Stereo-A EUVI at 195 Å images with cadence of 10-minute. From the SDO/AIA 193 Å perspective, we distinguish 338 CBPs in the mentioned region of interest.

Figure 4 illustrates the variation in the ability to track a CBP across the three instruments mentioned. As expected, the tracking ability of a given event in the EIT instrument is quite low. In the first row of Figure 4, greater scatter around the fitted line for the variations in solar latitude of a CBP over time (synodic velocity) is observed in the EIT data. This leads to an increase in the velocity calculation error, with the uncertainty in the velocity for EIT calculated as ± 0.4 $^{\circ}\text{day}^{-1}$. In contrast, the Stereo-A (second row) and AIA (third row) instruments show lower errors of ± 0.3 $^{\circ}\text{day}^{-1}$. This difference is related to the spatial resolution of the instruments; the EIT instrument has the lowest resolution of 2.4 arcseconds, while Stereo-A and AIA have resolutions of 1.2 and 0.6 arcseconds, respectively. Due to this difference in resolving power, the higher-resolution instruments were able to track the positional changes of the bright points with less noise and greater accuracy.

The meridional motion of a CBP in figure 4, observed simultaneously by SoHO/EIT, Stereo-A/EUVI, and SDO/AIA, shows clear differences in both direction and speed. All three instruments detected only slight changes in position over a 10-hour period, but with different movement patterns. SDO/AIA data show an almost flat path with a very slow speed of about 0.3 ± 0.1 $^{\circ}\text{day}^{-1}$, suggesting the CBP stayed nearly in the same latitude. In contrast, Stereo-A showed a stronger shift with a speed of about 1.1 ± 0.5 $^{\circ}\text{day}^{-1}$, and EIT recorded the largest motion at around 1.8 ± 0.5 $^{\circ}\text{day}^{-1}$. The CBP remained in low-latitude regions in all cases, indicating that short-term meridional movement is generally limited.

In this study, based on the data from the SoHO/EIT instrument, the synodic velocity of a CBP with the same spatial location as the other two instruments was estimated to be 14.98 $^{\circ}\text{day}^{-1}$. For the Stereo-A instrument, the synodic velocity was found to be 15.39 $^{\circ}\text{day}^{-1}$.

In the SDO/AIA data, the variation in latitude has a less scatter, and the spatial changes

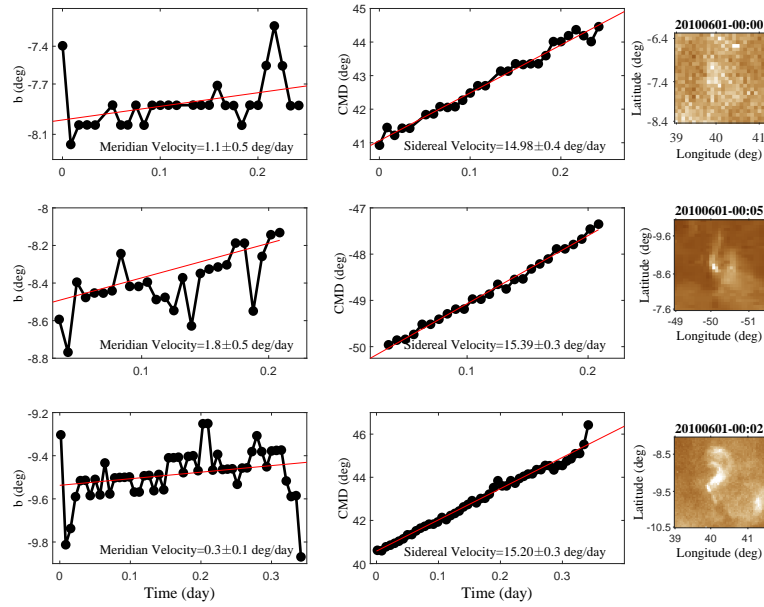


Figure 4: Figure shows the position of the same CBP as observed by the three instruments analyzed in this study. The middle panels display the sidereal rotation velocity, while the left panels represent the central meridian (longitudinal) velocity. These are almost at same time on June 1st, 2010.

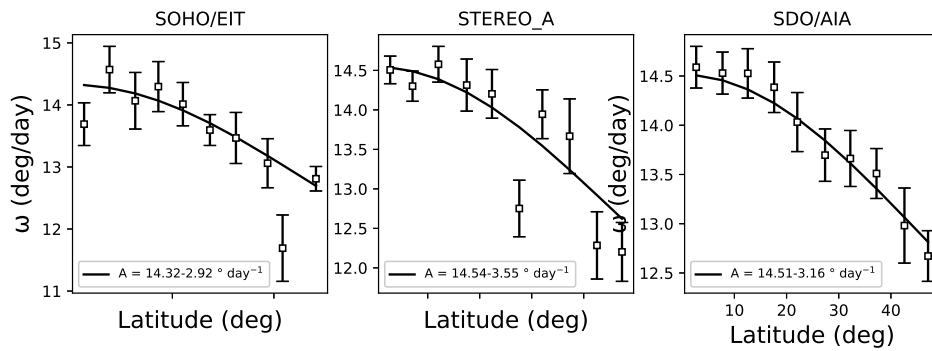


Figure 5: Sidereal rotation velocities derived for a single day from three instruments SoHO/EIT, Stereo-A/EUVI, and SDO/AIA. The calculation is based on Equation 19, with latitudinal binning applied every 10° .

of the event were tracked with greater stability. The synodic velocity calculated from this instrument was $15.20 \text{ }^\circ\text{day}^{-1}$, similar to the values reported in recent studies based on AIA data. For example, Sudar et al. (2016) estimated the average velocity of bright points in the range of 15.1 to $15.3 \text{ }^\circ\text{day}^{-1}$ [45]. The high spatial resolution of AIA (0.6 arcseconds), along with better image resolution, is the main reason for the increased accuracy in the results. According to the results presented in this study, the accuracy of measuring synodic and heliographic velocities clearly depends on the spatial resolution of the instrument and the quality of the images. In particular, the SDO/AIA instrument, due to its high resolution and more precise timing, has demonstrated the best performance in tracking CBPs. In contrast, the SoHO/EIT instrument, due to its resolution limitations and higher image errors, provided less accurate results.

Figure 5 shows the variation in the displacement of CBPs in solar latitude over time for one day and the first ten hours, with a temporal sampling rate of every ten minutes. The rotation parameters A and B obtained from the data analysis for each instrument are as follows: for SoHO/EIT data, the values of A were $14.32 \text{ }^\circ\text{day}^{-1}$ and B was $-2.93 \text{ }^\circ\text{day}^{-1}$. The corresponding values for Stereo-A were 14.54 and $-4.03 \text{ }^\circ\text{day}^{-1}$, and for SDO/AIA, they were 14.51 and $-3.16 \text{ }^\circ\text{day}^{-1}$. These slightly discrepancies in values of rotation parameters may related to the differences in data quality and temporal coverage from three instruments with different spatial and temporal resolution.

Overall, the limitations of the SoHO/EIT data, especially its irregular temporal sampling and the occasional presence of only one image per day, leading to significant investigation of solar rotation parameters for long period of study. In contrast, the high-quality data from Stereo-A/EUVI and particularly SDO/AIA have provided a more reliable and accurate analysis of the rotational behavior of these coronal phenomena.

5 Conclusion

In this study, the solar rotation was examined using the motion of coronal bright points (CBPs) observed by three different instruments: SoHO/EIT, Stereo-A/EUVI, and SDO/AIA. The results show that the accuracy of measuring solar rotation may depends on the spatial resolution and data quality of each instrument.

The SDO/AIA data provided the most stable and reliable tracking of CBPs, due to its high spatial resolution and regular time sampling. Stereo-A/EUVI also showed good performance, while SoHO/EIT data had more limitations. In particular, the low resolution and irregular time intervals of EIT images made it difficult to track CBPs accurately and led to larger errors in velocity calculations in longer periods.

The study also found that the measured velocities from different instruments varied slightly. These differences are mostly due to the instruments' technical characteristics, such as resolution and image timing. Overall, this analysis highlights the importance of using high-resolution and well-sampled data—like that from SDO/AIA—for accurate studies of solar rotation and the motion of small features such as CBPs.

Acknowledgment

We thank the SDO/AIA, Stereo-A/EUVI, and SoHo/EIT science teams for providing the data used here.

Authors' Contributions

All authors have the same contribution.

Data Availability

The data that support the findings of this study are available from the corresponding author upon reasonable request.

Conflicts of Interest

The authors declare no potential conflicts of interest.

Ethical Considerations

The authors have diligently addressed ethical concerns, such as informed consent, plagiarism, data fabrication, misconduct, falsification, double publication, redundancy, submission, and other related matters.

Funding

This research did not receive any grant from funding agencies in the public, commercial, or nonprofit sectors.

References

- [1] Brun, A. S., Miesch, M. S. & Toomre, J. 2004, *ApJ*, 614, 1073.
- [2] Browning, M. K., Miesch, M. S., Brun, A. S., & Toomre, J. 2006, *ApJ*, 648, L157.
- [3] Charbonneau, P. 2020, *Living Reviews in Sol. Phys.*, 17, 1.
- [4] Duvall, Thomas L. 1979, *Sol. Phys.*, 63, 3.
- [5] Xiang, N. B., Zhao, X. H., Deng, L. H., Li, F. Y., & Zheng, S. 2023, *Scientific Reports*, 13, 21089.
- [6] Mancuso, S., Giordano, S., Barghini, D., & Telloni, D. 2020, *A&A*, 644, A18.
- [7] Hathaway, David H., and A. J. Dessler. 1986, *Icarus*, 67, 88.
- [8] Brajša, R., Woehl, H., Vršnak, B., Ruždjak, V., Clette, F., & Hochedez, J. F. 2001, *A&A*, 374, 309.
- [9] Sudar, Davor, et al. 2015, *A&A*, 575, A63.
- [10] Howard, R., Gilman, P. I., & Gilman, P. A. 1984, Rotation of the sun measured from Mount Wilson white-light images. *Astrophysical Journal*, Part 1 (ISSN 0004-637X), 283, 373.
- [11] Li, K. J., Xu, J. C., Yin, Z. Q., & Feng, W. 2019, *ApJ*, 875, 90.

- [12] Chandra, S., Vats, H. O., & Iyer, K. N. 2009, MNRAS, 400, L34.
- [13] Sharma, J., Kumar, B., Malik, A. K., & Vats, H. O. 2021, MNRAS, 506, 4952.
- [14] Wu, Q. R., Zheng, S., Zeng, S. G., Wan, M., Zeng, X. Y., Deng, L. H., & Huang, Y. 2023, ApJ, 954, 20.
- [15] Deubner, F. L., Ulrich, R. K., & Rhodes Jr, E. J. 1979, A&A, 72, 177.
- [16] Wöhl, Hubertus, et al. 2010, A&A, 520, A29.
- [17] Li, F. Y., et al. 2019, ApJ, 873, 121.
- [18] Ataç, Tamer, and Atila Özgüç. 2006, Sol. Phys., 233, 139.
- [19] Joshi, Navin Chandra, et al. 2009, Sol. Phys., 260, 451.
- [20] Alipour, N, and H. Safari. 2015, ApJ, 807, 175.
- [21] Li, Jing. 2018, ApJ, 867, 89.
- [22] Shokri, Z, N. Alipour, H. Safari, P. Kayshap, O. Podladchikova, G. Nigro, and D. Tripathi. 2022, ApJ, 926, 42.
- [23] Shokri, Z., Alipour, N., & Safari, H. 2024, ApJ, 972, 46.
- [24] Alipour, N., H. Safari, and D. E. Innes. 2012, ApJ, 746, 12.
- [25] Lamb, Derek A. 2017, ApJ, 836, 10.
- [26] Madjarska, M. S. 2019, Living Reviews in Sol. Phys., 16, 2.
- [27] Bewsher, D., Parnell, C. E., & Harrison, R. A. 2002, Sol. Phys., 206, 21.
- [28] Sattarov, I., Pevtsov, A. A., Hojaev, A. S., & Sherdonov, C. T. 2002, ApJ, 564, 1042.
- [29] Javaherian, M., Safari, H., Amiri, A., & Ziaei, S. 2014, Sol. Phys., 289, 3969.
- [30] Yousefzadeh, M., Safari, H., Attie, R., & Alipour, N. 2016, Sol. Phys., 291, 29.
- [31] Rad, N. A., & Safari, H. 2012, IJPR, 12.
- [32] Honarbakhsh, L., Alipour, N., & Safari, H. 2016, Sol. Phys., 291, 941.
- [33] Alipour, N., Safari, H., Verbeeck, C., Berghmans, D., Auchère, F., et al. 2022, A&A, 663, A128.
- [34] Rad, S. H., Alipour, N., & Safari, H. 2021, ApJ, 906, 59.
- [35] Raboonik, A., Safari, H., Alipour, N., & Wheatland, M. S. 2016, ApJ, 834, 11.
- [36] Ghaderi, H., Alipour, N., & Safari, H. 2025, arXiv preprint arXiv:2501.09816.
- [37] Safari, H., Alipour, N., Ghaderi, H., & Garavand, P. 2023, Iranian J. Astron. Astrophys., 10, 267.
- [38] Vapnik, V. N. 1963, Automation and remote control, 24, 774.
- [39] Alipour, N., Mohammadi, F., & Safari, H. 2019, ApJSupplement Series, 243, 20.

- [40] Adams, R., & Bischof, L. 1994, IEEE Transactions on pattern analysis and machine intelligence, 16, 641.
- [41] Skokić, I., Brajša, R., Roša, D., Hržina, D., & Wöhl, H. 2014, Sol. Phys., 289, 1471.
- [42] Rosa, D., B. Vrsnak, and H. Bozic. 1995, Hvar Observatory Bulletin, 19, 23.
- [43] Vršnak, Bojan, et al. 1999, Sol. Phys., 185, 207.
- [44] Brajša, Roman, et al. 2004, A&A, 414, 707.
- [45] Sudar, Davor, et al. 2016, A&A, 587, A29.